International Journal of Medical, Medicine and Health Sciences
ISSN: 2517-9969
Vol:11, No:11, 2017

Iron(III)-Tosylate Doped PEDOT and PEG: A Nanoscale Conductivity Study of an Electrochemical System with Biosensing Applications

Giulio Rosati, Luciano Sappia, Rossana Madrid, Noemi Rozlòsnik

***Abstract*—**The addition of PEG of different molecular weights has important effects on the physical, electrical and electrochemical properties of iron(III)-tosylate doped PEDOT. This particular polymer can be easily spin coated over plastic discs, optimizing thickness and uniformity of the PEDOT-PEG films. The conductivity and morphological analysis of the hybrid PEDOT-PEG polymer by 4-point probe (4PP), 12-point probe (12PP), and conductive AFM (C-AFM) show strong effects of the PEG doping. Moreover, the conductive films kinetics at the nanoscale, in response to different bias voltages, change radically depending on the PEG molecular weight. The hybrid conductive films show also interesting electrochemical properties, making the PEDOT PEG doping appealing for biosensing applications both for EIS-based and amperometric affinity/catalytic biosensors.

***Keywords*—**Atomic force microscopy, biosensors, four-point probe, nano-films, PEDOT.

I. Introduction

FOR several years, the impact of conducting polymers (CPs) has increased in all kinds of technological applications. These materials are very interesting within the fields of organic electronics and bioengineering due to their low-cost, flexibility and ease of manufacturing on conductive and non-conductive substrates [1]. The CPs are versatile materials since their properties can be easily modulated by the most common surface functionalization techniques, and a wide range of molecules can be incorporated to the structure of the films to further functionalize them or act as dopants improving the conductivity of the polymer itself [2].

Among many CPs, poly(3,4 ethylene dioxythiophene) (PEDOT) has been one of the most studied and used due to its long term stability in air, low cost for mass production, high conductivity and desirable electro-optical properties. This polymer has several applications in the development of OLEDS [3], [4], lithium batteries [5], [6], supercapacitors [7]-[9], and biosensors [10]-[13].

Giulio Rosati (Dr) is with the Department of Information Engineering, University of Padova Via G. Gradenigo 6/b, 35131, Padova, Italy (corresponding author, e-mail: rosatigiulio@gmail.com).

Noemi Rozlòsnik (Prof. Dr.) is with Department of Micro- and Nano-technology, Danish Technical University, Kgs. Lyngby 2800, Copenhagen, Denmark.

Luciano Sappia and Rossana Madrid[2] are with the Laboratorio de Medios e Interfases, Departamento de Bioingeniería, Fac. de Cs. Exactas y Tecnología, Universidad Nacional de Tucumán, Av. Independencia 1800, 4000 San Miguel de Tucumán, Argentina, and the Instituto Superior de Investigaciones Biológicas, CONICET, Chacabuco 461, T4000ILI San Miguel de Tucumán, Argentina.

PEDOT films can be deposited by three main pathways, i.e., electrochemical polymerization (EP) [14]-[16], chemical oxidation polymerization (COP) [17]-[19], and Vapor Phase Polymerization (VPP) [20], [21]. In this work, we focus on the COP method, which allows the use of nonconductive substrates. In order to balance charges in the polymer's backbone and improve conductivity, counter-anions are used to dope the PEDOT. The most common dopants found in the literature are polystyrene sulphonate (PSS) [22]-[25] and iron/sodium tosylate salts [26], [31].

In order to enhance the conductivity of PEDOT films, different strategies were explored, including the addition of nonconductive co-polymers and post-deposition treatments. In the case of PEDOT:PSS films, copolymerization was done adding ethylene glycol (EG) and diethylene glycol (DEG). Post-deposition treatments were performed by immersion of the films in EG [22] or formic acid [23] baths.

Conversely, PEDOT:Tos films were copolymerized with polyethylene glycol (PEG) and PEG *ran* polypropylene glycol (PPG), as described in Table I.

The incorporation of PEG-ran-PPG copolymer to PEDOT:Tos films deposited by spin-coating does not seem to affect the crystallinity of the polymer, but changes in the morphology were observed by SEM [32].

In this work, we investigate the effects of PEG as co-polymer of PEDOT:Tos films deposited by spin-coating. Electrical, morphological, and nanoscale conductivity properties of PEDOT/PEG composites are compared with pristine PEDOT films. Differently from the previous works on this topic, we chose to change only the PEG molecular weight (MW), from 20 kDa (the maximum MW reported in literature) down to 1.5 kDa, keeping constant the molarity of added PEG. As suggested by a previous work [26], a PEG molar ratio of 1.62 μM in 1 ml of oxidant solution was used. The film deposition protocol was optimized in terms of uniformity on the plastic substrates. Then, we investigated the films electrical/morphological properties by 4PP, 12PP, AFM, conductive-AFM, and cyclic voltammetry. A detailed study of the rectification effect of the composites was carried out applying bias voltage sweeps in order to study the influence of different PEG molecular weights. Our results suggest that 1.5 kDa PEG copolymer produces the smoothest films, with a homogeneous conductivity at the nanometer scale, and the highest rectification effect, with an applied bias voltage between -1 and +1 V.

TABLE I
COPOLYMERS USED IN PEDOT:PSS AND PEDOT:TOS FILMS

CP	Co-polymer	Polymerization method	Treatment and copolymer added	Reference
PEDOT:PSS	EG	VPP	6% v/v EG of the Oxidant solution	[22]
	EG + EG bath	VPP	Annealing and EG bath (30 min)	[22]
	DEG	COP / Spin coating	DEG 5 wt.%	[24]
	D-Sorbitol	Spin coating	3 wt.%	[25]
	Glycerol	Spin coating	4 wt.%	
	EG	Spin coating	1:1 v/v	
	DMSO	Spin coating	3:1 v/v	
	-	Spin coating	Annealing and formic acid immersion	[23]
PEDOT:Tos	PEG	COP / Spin coating	Addition of 33 mg of PEG 20 kDa per mL of Baytron C	[26]
	PEG	VPP	PEG 20 kDa added to oxidant solution (30%, 50% and 70% PEG/ PEDOT)	[27]
	PEG ran PPG	VPP	5 wt. % PEG-ran-PPG	[28], [29]
PEDOT:OTf	PEG-PPG-PEG	COP/spin coating	Sulfuric acid bath for 30 minutes	[30], [31]

VPP: Vapor Phase Polymerization, COP: Chemical Oxidation Polymerization, EG: Ethylene glycol, DEG: Diethylene glycol, PEG: Poly ethylene glycol, PEG ran PPG: Poly Ethylene Glycol / Poly Propylene Glycol. OTf: iron (III) trifluoromethanesulfonate

II. MATERIALS AND METHODS

A. Films Deposition by Spin Coating

In order to investigate the surface properties of iron(III)-tosylate doped PEDOT-PEG mixtures, the material was chemically polymerized on injection moulded (Victory 80/45 Tech, Engel, Germany) cyclic olefin copolymer (COC) TOPAS 5013S-04 discs (TOPAS Advanced Polymer, Germany, Tg=134 °C) with a diameter of 50.8 mm and a thickness of 2 mm. The deposition of the PEDOT-PEG mixtures was achieved by spin coating. The deposition protocol for the PEDOT with no PEG addition (pristine PEDOT:Tos films) consisted in the spin coating (speed: 800 rpm, acceleration: 400 rpm/s) of 362 µl of a solution containing 8.8 µL of the monomer (EDOT), 260 µL of Baytron C (40% iron(III) tosylate in butanol), 80 µL of butanol and 6 µL of pyridine to inhibit the spontaneous polymerization. Then, the spun discs were heated to 90 °C to evaporate the pyridine inhibitor and to start the polymerization of the EDOT monomer. The polymerization was complete in less than 5 minutes, with an evident color change from clear to dark green, as shown in Fig. 1. The last preparation step was the disc washing with ultrapure water, accompanied by a color change of the discs to clear blue.

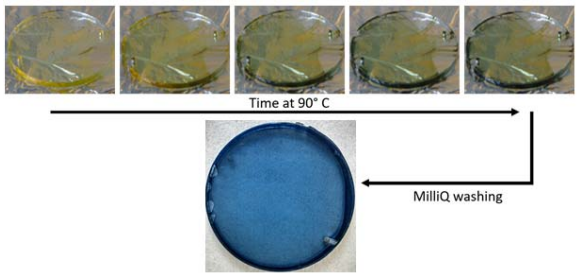

Fig. 1 Color change during the spun discs heating due to the EDOT polymerization and disc obtained after the ultrapure water washing (Milli-Q, Merk-Millipore, USA) to remove the excess of Fe^{3+} ion

PEG average molecular weights from 1.5 to 20 kDa were used, maintaining constant the ratio with the oxidant solution. We chose not to test PEG molecular weights over 20 kDa because of the low conductivity obtained with that MW (Fig. 7), and also because of the lack of comparison with analogous results in literature.

The PEDOT-PEG polymer film mix was always performed with the same protocol, i.e. PEG powder was dissolved in 400 µl of ultrapure water (Milli-Q, Merk-Millipore, USA), and then heated at 30 °C for 5 minutes. In the meantime, the Baytron C, butanol and pyridine (denoted as oxidant solution) was prepared with the described ratios.

The PEG solution was mixed with the oxidant solution, then the monomer EDOT was added. Finally, the obtained solution was filtered with a 0.22-µm porous membrane to remove any potential monomer agglomerate, which could affect the nano-film uniformity. The preparation protocol is described in Table II for the different PEG MWs.

The spin coating parameters were optimized in order to produce uniform nano-films on the TOPAS discs, as shown in Fig. 2 for PEDOT:PEG 6 kDa.

A speed of 800 rpm for 60 s and an acceleration of 400 rpm/s resulted optimal for the spin coating. Therefore, three discs per each PEG MW were prepared. The spun discs were marked with the letters A, B, C, D, E and by the disc number on the back, as represented in Table II. These letters will be used in the following as disc identifier.

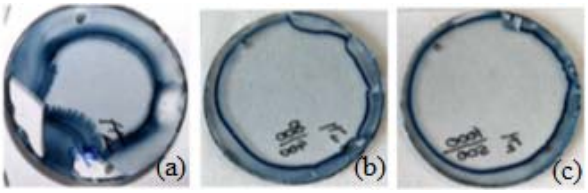

Fig. 2 Spin coating parameters optimization results for the deposition of a PEDOT layer with PEG 6 kDa 1.45 M/ml of Baytron C used in the oxidant solution. The spinning time has been kept constant (60 s) The used accelerations and speed are: a) 250 rpm/s, 500 rpm; b) 400 rpm/s, 800 rpm; c) 500 rpm/s, 1000 rpm

TABLE II
AMOUNTS OF PEG, EDOT AND OXIDANT SOLUTION USED TO PRODUCE THE PEDOT:PEG MIXTURES

Disc name	PEG molecular weight (kDa)	PEG mass (mg)	Oxidant solution volume (µl)	EDOT volume (µl)
A	0 (normal PEDOT:Tos)	0	951.5	12.1
B	20	23.6		
C	6	7.08		
D	3	3.54		
E	1.5	1.77		

B. Conductivity Measurements

The conductivity tests on the spun discs were carried out by 4-point probe (4PP) and 12-point probe (12PP) measurements. The formers were performed on five points over the whole discs' surface, as showed in Fig. 3 inset for the A1 disc. Ten logarithmically-spaced current values were applied for each tested point. The respective surface resistance values were measured.

Conversely, the 12PP measurements were performed only at the center of each spun disc, by a Capres A/S M12PP micro-fabricated tip.

In order to calculate the material conductivity, the nano-film thickness was measured by contact mode atomic force microscopy (AFM) across the border of a scratch of the PEDOT:PEG nano-film.

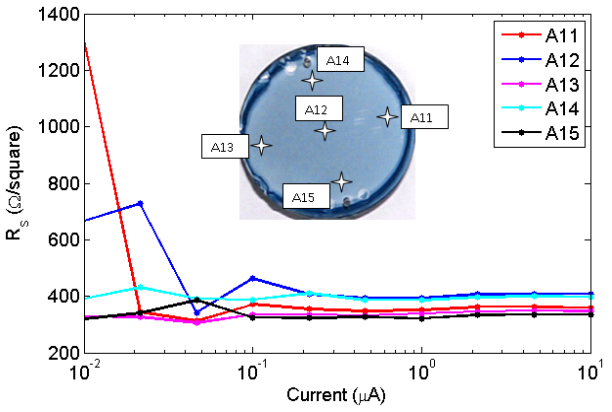

Fig. 3 4PP measurements performed on the disc A1 in the five points indicated in the inset of the plot

C. Morphological and Conducting AFM

The morphology of the A, C and E discs was characterized by AFM in contact mode configuration in a square area of 25 μm^2. The nanoscale conductance of the discs was measured in the same area by conducting AFM (C-AFM), connecting the disc surface to a gold clip and applying a fixed potential between the AFM tip and the clip. The current flowing through the disc surface was amplified and converted in a tension by a current-voltage amplifier, as shown in Fig. 4.

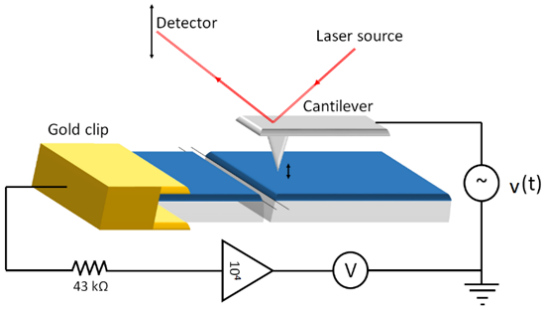

Fig. 4 Scheme of the conducting AFM measurements system. The components depicted here are not in scale

To obtain the discs current-voltage characteristics, other conducting AFM measurements were performed applying tensions from -1.1 V to 1.1 V with a step of 0.1 V during the tip scan. The current-voltage characteristics of the discs, were calculated by averaging the current values measured in the discs' areas related to each applied tension value. All the AFM and C-AFM data were analyzed by Gwyddion 2.44 software.

D. Switching C-AFM

In order to disclose the discs' nanometer scale response to the voltage switching, a square wave tension was applied during the tip scan, switching the potential from a positive value to the corresponding negative value, and then back to the positive one (Fig. 5). The amplitude of the square wave from zero was varied from 0.1 V to 1.1 V with 0.1 V steps, obtaining the A, C, E current responses over time (and space). The discs' current-voltage characteristics were calculated by averaging the values corresponding to the positive and the negative tensions areas in the switching C-AFM images.

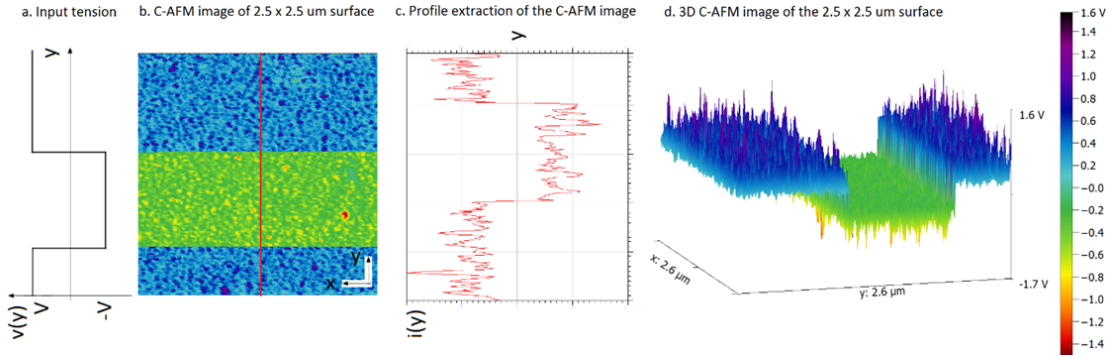

Fig. 5 Switching C-AFM example. From right to left: input tension signal (a), C-AFM recorded image with colors referred to the color scale on the left (b), current profile extracted from the C-AFM image and converted to current (c), 3D C-AFM image (d)

E. Cyclic Voltammetry

The PEDOT:PEG conductive films were further characterized by Cyclic Voltammetry (CV). The measurements setup consisted of a microfluidic electrochemical cell (sketched in Fig. 6), realized by covering a patterned PEDOT:PEG disc with bi-adhesive tape to create a microfluidic channel over the conductive layer. Then, the device was closed by a TOPAS cover with Luer-compliant connections for the testing solution injection and conducting layer contact. A standard counter and reference electrodes set was built. The counter electrode was obtained by inserting a platinum wire in a Luer connector, while the reference electrode was made by placing an Ag/AgCl wire in a 1-M KCl filled tubing, hosted in a Luer connector with a porous glass membrane end, as shown in Fig. 6. A gold Luer connector was used to contact the conductive layer and close the electrochemical cell. Phosphate Buffered Saline (PBS) was used as supporting electrolyte without the addition of any redox mediator, with the aim to observe only the reduction and oxidation peaks of the doped PEDOT. The CV measurements were performed with a scan rate of 100 mV/s, between -0.9 V and + 0.9 V.

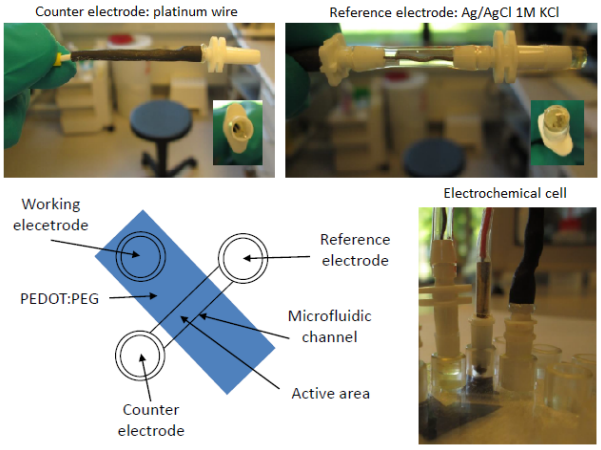

Fig. 6 Standard platinum wire counter electrode and Ag/AgCl reference electrodes used to setup the electrochemical cell sketched in the bottom left schematics and showed in the bottom right picture

III. Results

A. Conductivity Measurements

The 4PP and 12PP results are summarized in Table III, together with the average thicknesses measured on the nano-films by AFM. The conductivities have been calculated with the following equation:

$$\sigma = 1 / R_s\, t \qquad (1)$$

with R_s, the sheet resistance, measured by 4PP or 12PP and t is the thickness of the discs' conductive layers. The average sheet resistances measured by 4PP are plotted in Fig. 7. The figure inset compares the conductivities calculated from the 4PP and the 12PP measurements.

TABLE III
AVERAGE 4PP SURFACE RESISTANCE VALUES, AFM-MEASURED NANO-FILM THICKNESSES, AND CONDUCTIVITY VALUES OBTAINED FROM THE DISCS PER EACH TESTED SOLUTION, BY 4PP AND 12PP

Disc name	PEG m.w. (kDa)	Thickness (nm)	4PP Surface resistance (Ωsq)	σ_{4PP} (S/m)	σ_{12PP} (S/m)
A	0	76.3 ± 4.9	351 ± 32	37663.9 ± 3632.5	27748.7± 3832.4
B	20	20.3 ± 2.7	14605 ± 5179	3726.5 ± 974.1	3415.7 ± 158.3
C	6	34.9 ± 4.3	1192 ± 247	26285.3 ± 8255.5	19788.2 ± 900.1
D	3	29.9 ± 3.5	1232 ± 140	27379.8 ± 3206.4	21866.5 ± 5480.0
E	1.5	42.0 ± 2.4	1236 ± 214	20332.0 ± 3836.6	17788.3 ±46.5

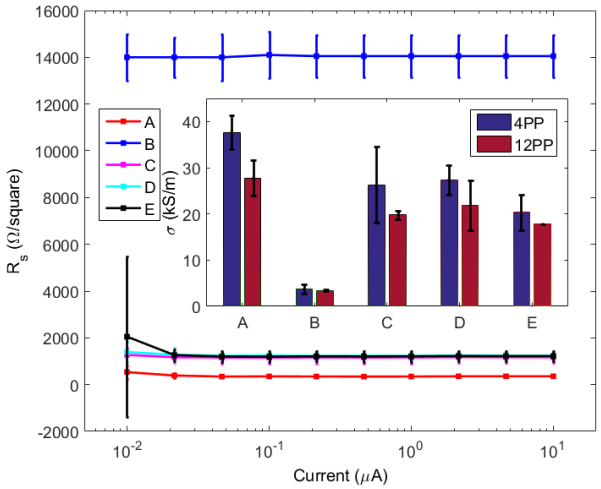

Fig. 7 Sheet resistances mean values and standard deviations measured by 4PP on the spun discs. In the inset, the 4PP calculated conductivities are compared to the 12PP ones

The 4PP and 12PP results are coherent in most cases. Generally, the 12PP ones have slightly lower average values. The PEG addition to the PEDOT formulation seems not to improve the conductivity of the material. However, the C, D and E discs show conductivity values similar to normal PEDOT ones (A discs). Conversely, B discs show very low conductivity, and have been excluded from further tests and analysis. The low conductivity of the B discs is surprising since PEG 20 kDa has been used in several works for the PEDOT:Tos conductivity enhancement [26], [27]. However, those works used much higher PEG concentrations than us and different deposition techniques.

Since the results obtained from the C and D discs are very similar, only the A, C, E discs have been further characterized by AFM and C-AFM.

B. Morphological and Conducting AFM

The morphological and conducting AFM measurements were performed with the setup depicted in Fig. 4. The results, obtained over a square of 5 x 5 µm, are represented in Fig. 8 for the A, C, and E discs. The morphology and the conductivity of the discs' surface are shown both by 2D and 3D images. This allows to appreciate the average roughness

and the presence of micrometric and sub-micrometric structures in the morphology images. Regarding the C-AFM, the uniformity of conduction at -0.3 V is shown by the 2D images, while the 3D plots highlight the huge differences between the devices' conduction (by both the peak heights and colors), measured as a tension by the setup of Fig. 4. These measurements clearly show a PEG smoothing effect on the film surfaces. This effect, particularly evident from the 3D plots on the right in Fig. 8, depends on the PEG molecular weight, with smoother surfaces corresponding to lower PEG molecular weights. As it was reported by Jimison et al. [27], the addition of PEG copolymer suppresses the formation of micro-scale domains, providing a smoother energetic landscape for charge transport. Also, the nanoscale conductivity of the surface appears strongly influenced by the PEG addition and by its molecular weight. In fact, the uniformity and the amplitude of the measured tension are greater for lower PEG molecular weights (as showed in Fig. 9 3D plots on the left). Therefore, from the AFM and C-AFM analysis, the E discs have the best morphological uniformity and the highest conductivity.

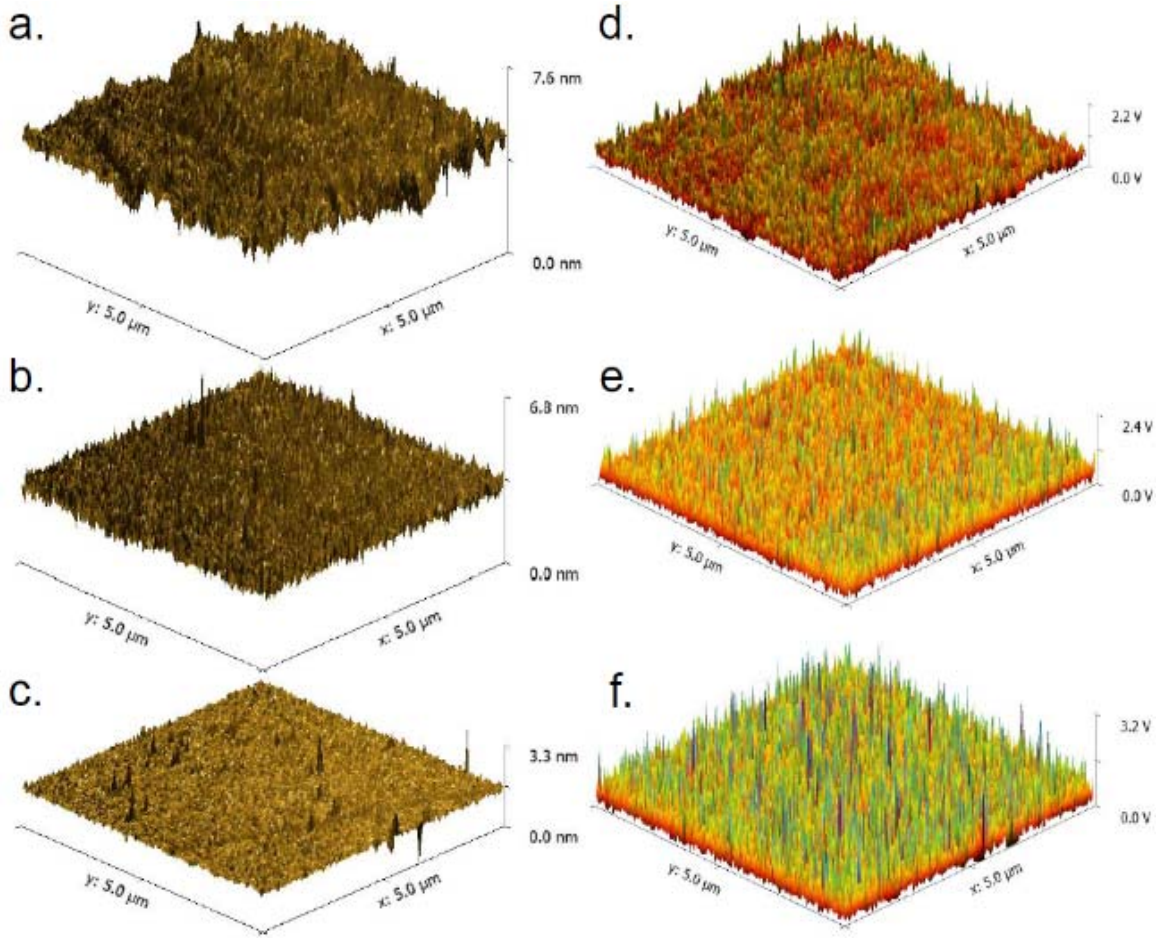

Fig. 8 2D and 3D morphological (a,b,c) and conducting (d,e,f) AFM responses at -0.3 V of the A, C, E discs respectively from the top to the bottom (5 x 5 µm). The conducting images have been referred to the voltage scale reported on the right

The actual roughness, the maximum height, depth and peak height of the AFM measured discs are shown in Fig. 9. The roughness of the normal PEDOT resulted 4 times reduced by the addition of PEG 1.5 kDa (E discs), with an RMS roughness value below 100 pm. The same ratio was found also for the other geometrical characteristics between the A and the E discs.

As described in paragraph II.C, C-AFM measurements were performed changing the tip voltage from -1.1 to +1.1 V during the surface scan. We obtained images like the inset of Fig. 10. Then, we calculated the current values by averaging the area of the images related to each applied tension. Thus, we obtained the current-voltage characteristics. These are depicted in Fig. 10 for the A, C, E discs. All the curves are characterized by a reduction peak close to -0.5 V and show a rectifying effect with low or no conductance at lower tensions. Slight differences are observed between the discs at these tensions. For positive tensions, the currents have a bilinear characteristic with a lower slope between zero and 0.6 V. Again, the E discs show a strong increase of the current at

positive tensions with respect to the others.

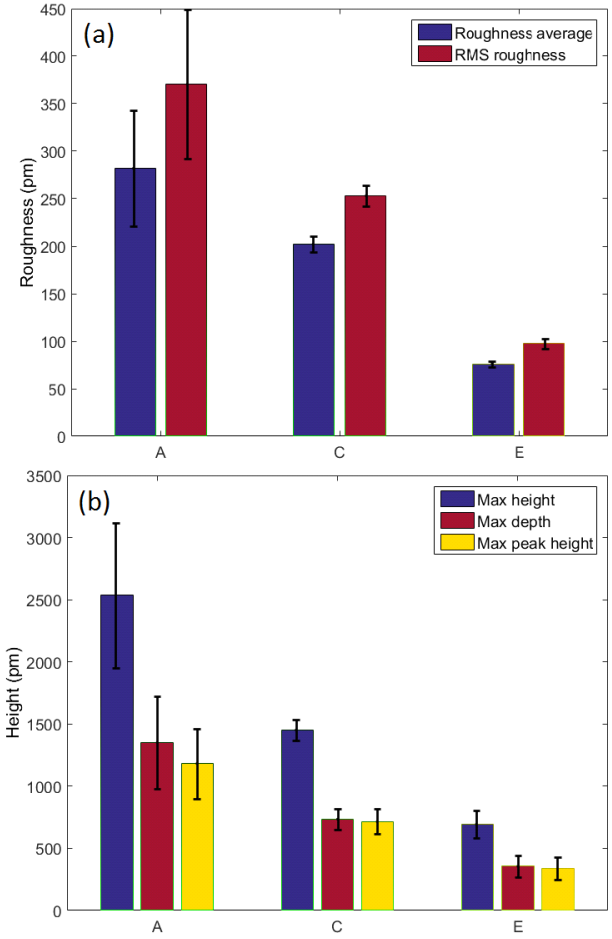

Fig. 9 Roughness (a) and geometrical (b) characteristics extracted from the AFM morphological data of the A, C, E discs

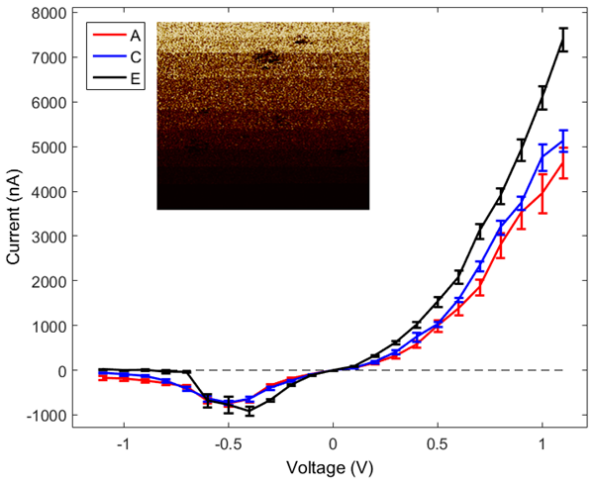

Fig. 10 Current-voltage characteristics of the A, C, E discs, measured by C-AFM from -1.1 V to 1.1 V with a 0.1-V step during the scan. The inset shows an example of the C-AFM images obtained and used to calculate the characteristic points

C. Switching C-AFM

The images obtained by the switching C-AFM measurements on the A, C, E discs (e.g. the picture in Fig. 5) were analyzed extracting the profiles of the current change in response to the tension switch. The A, C, E discs' profiles are represented in Fig. 11 for all the tested voltages. All the profiles were rescaled converting the C-AFM spatial coordinates in time, calculated on the basis of the C-AFM tip scan path and speed.

The data in Fig. 11 show a clear time dependence, thus the negative to positive voltage transitions were fitted by a biased exponential function:

$$y(t) = c + Ae^{-bt} \quad (2)$$

The data points and the respective fits are reported in the bottom right plot of Fig. 11 for the 1.1 V applied tension. The comparison clearly shows that the current switching dynamic of the E discs is different from that one of the A and C one. Fig. 12 shows the values of the A, b, c parameters obtained from the fits as a function of the applied tension.

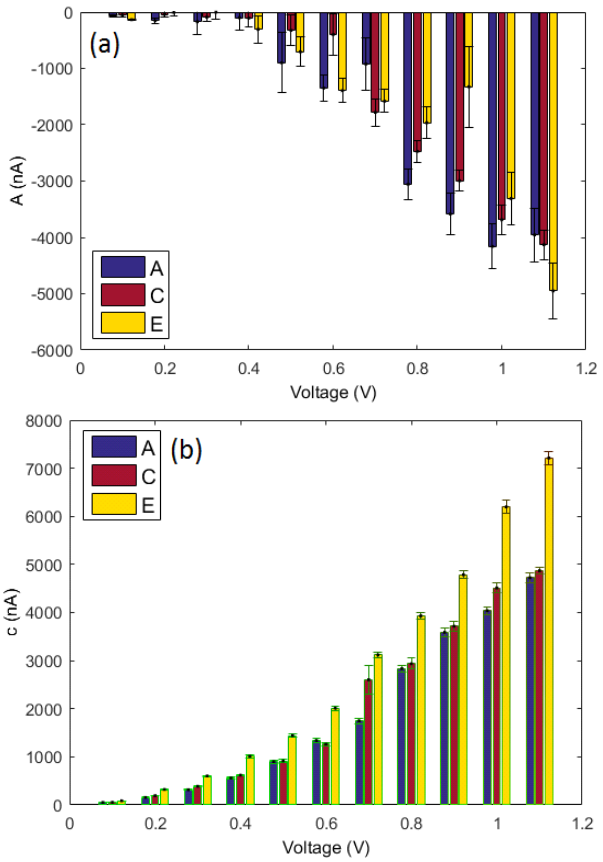

Fig. 12 Exponential fits amplitude (a) and bias (b), of the transitions from the negative to the positive tensions of the A, C, E discs. The error bars represent the 95% confidence interval of the fitted values. The time constant parameter trend is discussed in the following

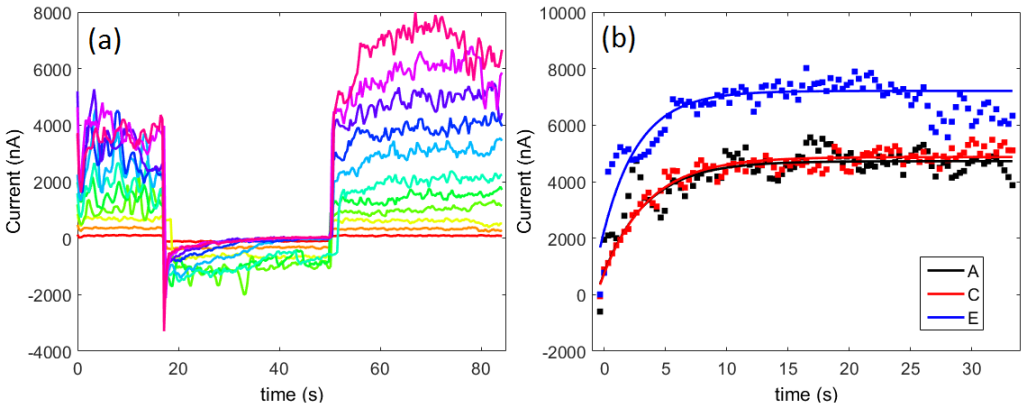

Fig. 11 Current profiles extracted from the switching C-AFM images at different tensions for C discs (a) and comparison of the current values extracted from the switch at 1.1 V (b) and the respective fits for the three discs (the time axis has been opportunely rescaled)

The exponential amplitude parameter (A) shows a module increasing trend with respect to the applied tension. However, no significant differences are observed between the A, C, E discs. Conversely, the current bias (c) value increases with the applied tension, and the E discs clearly show higher values than the other discs.

Regarding the increase rate (b) of the exponential fit, the reciprocal of this parameter has a more interesting significance as it is the time constant of the exponential function.

The 1/b trend is showed in Fig. 13. The values seem to depend on the applied tension for all the discs, with faster responses to the tension switch below 0.7 V and slower responses for tensions above that value. Moreover, along both the tension intervals, the time constant is bell-shaped for all the tested discs.

In the higher tension region, the E discs showed the fastest response since their time constant is smaller. The A discs showed slightly higher values while, surprisingly, the C discs showed very high values, and thus a slower response time than both A and E discs.

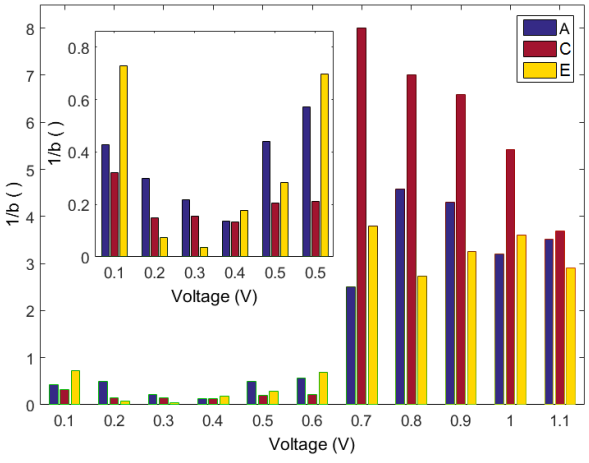

Fig. 13 Time constant plot (reciprocal of the fitted b value) as a function of the switching C-AFM applied voltage. The inset shows a magnification of the data below 0.6 V. The thick lines represent data interpolation to guide the eye

The tension at which the time constants radically change corresponds to the tension at which the current voltage characteristics of the discs (Fig. 10) increased their slope.

A possible explanation of these phenomena is illustrated in Fig. 14. Our hypothesis is that the films behavior with voltages above 0.7 and below -0.7 V, are dominated by electrostatic attraction and repulsion of the tosylate anions with negative charge. Indeed, high positive voltage could attract negative tosylate ions, increasing the conductivity of the material by a doping/undoping local process. The opposite behavior is observed with negative voltages below -0.7 V, where the conductivity of the material, in terms of the net value of the current, drops almost to zero. The attraction of tosylate anions with positive voltages could also cause the increase of the time constant of the transition from negative to positive voltages (Fig. 13). In fact, in this case the conduction would become predominantly mediated by the anions instead by the PEDOT chains. The presence of PEG in the PEDOT film and its chain length influence this conduction mechanism, probably changing the mobility of tosylate anions in the film. However, this hypothesis has not been proved yet and requires additional experiments and simulations to be confirmed.

Based on the structure of the composite shown in Fig. 14, the mobility of the counter-anions from the backbone of the polymer would have more mobility from the polymer when the different voltages are applied to the surface by the AFM tip. This could be explained why the time constants found for A (Pristine PEDOT:TOS) and E (PEDOT:TOS:PEG1500) have the same behavior. In the case of C (PEDOT:TOS:PEG6000), the presence of longer chains of PEG in the structure of the polymer could act as a barrier for tosylate ions mobility from the backbone of the PEDOT chains.

D.Cyclic Voltammetry

The CV measurements were performed on all the discs in triplicate. The tension range was -0.9 V – +0.9 V with a scan rate of 100 mV/s to avoid the PEDOT:Tos over oxidation. All the CV presented a reduction peak between -0.5 V and -0.6 V and a much smaller oxidation peak between 0.5 V and 0.7 V.

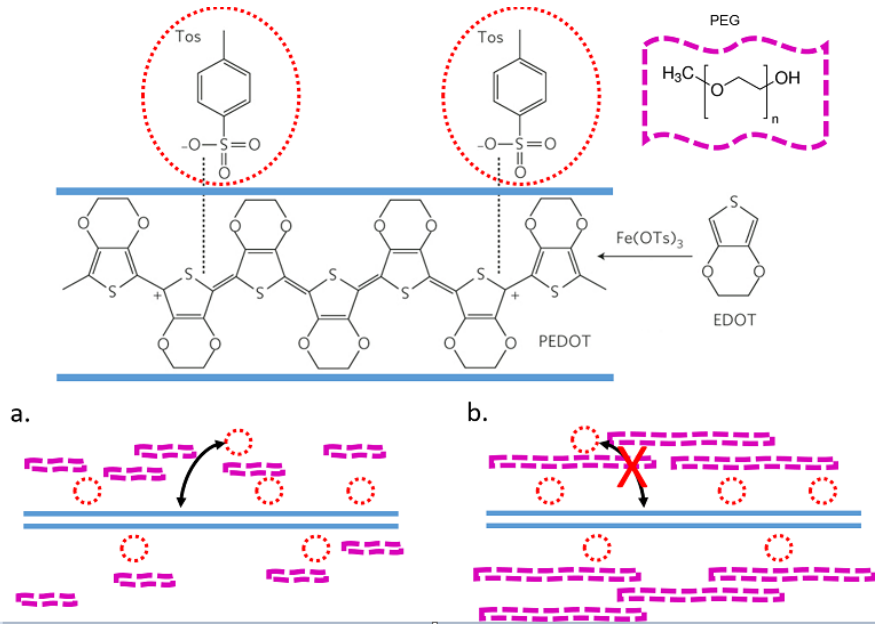

Fig. 14 PEDOT:Tos + PEG structure. The cases (a) and (b) show the hypothesized effect of different molecular weight PEG on the tosylate anions mobility at voltages above 0.7 or below -0.7 V

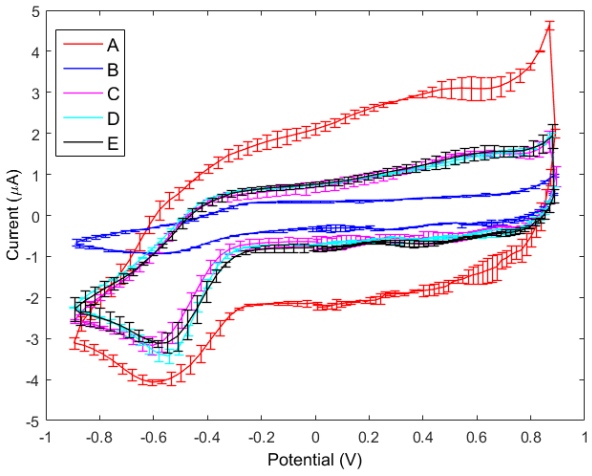

Fig. 15 Cyclic voltammograms of the A, B, C, D, E discs recorded on 20 mm^2 electrodes in PBS

However, the overall capacitance is calculated as the area under the curve resulted higher than all the other discs. The B discs presented the lowest capacitance value but also very low peak currents. Conversely, the C, D, E discs showed almost superimposed CV curves with a reduction peak very close to normal PEDOT, and reduced capacitance values.

Reduced capacitance values are important for EIS-based affinity biosensors. In fact, they imply a higher capacitive impedance. Thus, the double layer capacitance contribution becomes visible at higher frequencies in the EIS spectra. This means faster response times of the biosensor and less limitations on the conductivity of the solution to be tested. These considerations have been deepened by Rosati et al. in 2014 [34] proposing an analytical method for the design of interdigitated PEDOT:Tos microelectrodes for EIS-based microfluidic biosensors. This method basically relies both on the conductivity of the solution to be tested and on the conductive polymer conductivity to optimize the sensitivity of the EIS measurements to the electrodes surface state.

Reduced capacitance values are also important for catalytic enzyme-based biosensors. In this case, lowering the capacitance of the system allows increasing the sensitivity of the sensor to the charge transfer phenomena occurring at the interface, obtaining a better noise and interferences rejection in proximity of the current peaks of the voltammograms and of the amperometric curves. Moreover, the capacitance reduction lowers the recovery time of the biosensor.

IV. Conclusions

In this work, we studied PEDOT tosylate thin film electrodes modification by PEG at different molecular weights. We optimized the film deposition protocol using spin coating on TOPAS polymeric substrates. Then, we characterized the film sheet resistance and thickness by 4PP, 12PP, and AFM. From these measurements, we calculated the films conductivities, proving that the PEG molecular weight strongly influences the PEDOT:Tos conductivity. Moreover, we found a PEDOT:Tos+PEG formulation to obtain a conductivity similar to basic PEDOT:Tos, but with a very flat surface (RMS roughness <100 pm).

We characterized also the films conductivity at the nanoscale by conducting C-AFM, finding a much more uniform spatial conduction of the films with respect to basic PEDOT:Tos. After that, we obtained the conductive films current-voltage characteristics, identifying the reduction and oxidation potentials, and observing the PEDOT:Tos rectifying effect. At positive potentials, we found that

PEDOT:Tos:PEG1500 Da is more conductive than pristine PEDOT:Tos.

The main point of our work was the study of the nanoscale current kinetics in response to applied tension switching by C-AFM. We observed that the kinetics depend both on the applied tension and on the PEG molecular weight. At potentials over 0.6 V, PEDOT:Tos+PEG 1500 Da showed the fastest response, while the slowest one was the PEDOT:Tos+PEG 6000 Da one. At lower positive potentials the situation is inverted, with PEDOT:Tos+PEG 6000 Da giving the best kinetic performance.

Finally, we tested the conductive films by CV measurements, confirming the previous characterizations' results, and showing the implementation of a possible setup for the use of these devices for biosensing applications.

Other works with these materials showed promising and interesting results in the realization of electrochemical biosensors for the detection of the Influenza A virus [33], of antibiotics like Ampicillin [34] and of other important biomolecules by impedimetric measurements. However, the improvement of the material conductivity at the nanoscale performed in this work gives useful insights on how these materials can be used to obtain better performances in both catalytic and affinity biosensing applications.

ACKNOWLEDGMENT

L. S. gratefully acknowledge CONICET for the scholarship. R. M is a staff researcher of CONICET.

REFERENCES

[1] S. Hideki, E. J. Louis, A. G. Macdiarmid, C. K. Chiang, A. J. Heeger, Chem. Commun. 1977, 578.
[2] A. J. Heeger, Angew. Chem. Int. Ed Engl. 2001, 40, 2591.
[3] W. H. Kim, A. J. Mäkinen, N. Nikolov, R. Shashidhar, H. Kim and Z. H. Kafafi, *Appl. Phys. Lett.* 2002, *80*, 3844.
[4] G. F. Wang, X. M. Tao, R. X. Wang. G. F. Wang, X. M. Tao, and R. X. Wang, *Composites Science and Technology*. 2008, *68*, 14, 2837.
[5] D. T. Jr. Hallinan, S. A. Mullin, G. M. Stone and N. P. Balsara, *J. Electrochem. Soc.*, 2013, *160*, 3, A464.
[6] G. Ma, Z. Wen, Q. Wang, C. Shen, J. Jin and X. Wu, *J. Mater. Chem. A*, 2014, *2*, 19355.
[7] K. S. Ryu, Y.-G. Lee, Y.-S. Hong, Y. J. Park, X. Wu, K. M. Kim, M. G. Kang, N.-G. Park, S. H. Chang, *Electrochimica Acta*. 2004, *50*, 2–3, 30, 843.
[8] D. Antiohos, G. Folkes, P. Sherrell, S. Ashraf, G. G. Wallace, P. Aitchison, A. T. Harris, J. Chen and A. I. Minett, *J. Mater. Chem.* 2011, *21*, 15987.
[9] A. M. Österholm, D. E. Shen, A. L. Dyer, and J. R. Reynolds, *ACS Appl. Mater. Interfaces.* 2013, *5*, 24, 13432.
[10] G. Istamboulie, T. Sikora, E. Jubete, E. Ochoteco, J.-L. Marty, T. Noguer, *Talanta*. 2010, *82*, 3, 957.
[11] R. A. Olowu, O. Arotiba, S. N. Mailu, T. T. Waryo, P. Baker and E. Iwuoha, *Sensors (Basel)*. 2010, *10*, 11, 9872.
[12] J. Daprà, L. H. Lauridsen, A. Toftgaard Nielsen, N. Rozlosnik, *Biosensors and Bioelectronics*, 2013, *43*, 315.
[13] A. Phongphut, C. Sriprachuabwong, A. Wisitsoraat, A. Tuantranont, S. Prichanont, P. Sritongkham, *Sensors and Actuators B: Chemical*. 2013, *178*, 501.
[14] A. Aleshin, R. Kiebooms, R. Menon, and A. J. Heeger, *Synth Met*, 1997, *90*, 1, 61.
[15] T. El Moustafid, R. V. Gregory, K. R. Brenneman, and P. M. Lessner, *Polymer Preprints*. 2002, *43*, 2, 1320.
[16] G. Zotti, S. Zecchin, G. Schiavon, F. Louwet, L. Groenendaal, X. Crispin, W. Osikowicz, W. Salaneck, M. Fahlman, *Macromolecules*. 2003, *36*, 3337.
[17] F. Jonas, G. Heywang and W. Schmidtberg (Bayer AG) *DE 38 13 589*, 1988.
[18] L. Pettersson, F. Carlsson, O. Inganas, H. J. Arwin, *Thin Solid Films*. 1998, *313-314*, 356.
[19] B. Winther-Jensen, D. W. Breiby and K. West, *Synth. Met.* 2005, *152*, 1-3, 1.
[20] J. Kim, E. Kim, Y. Won, H. Lee, K. Suh, *J. Synth. Met.* 2003, *139*, 485.
[21] B. Winther-Jensen and K. West., *Macromolecules*. 2004, *37*, 4538.
[22] Y. H. Kim, C. Sachse, M. L. Machala, C. May, L. Müller-Meskamp, K. Leo, *Adv. Funct. Mat.* 2011, *21*, 6, 1076.
[23] D. A. Mengistie, M. A. Ibrahem, P.-C. Wang, and C.-W. Chu, *ACS Appl. Mater. Interfaces*. 2014, *6*, 4, 2292.
[24] X. Crispin, F. L. E. Jakobsson, A. Crispin, P. C. M. Grim, P. Andersson, A. Volodin, C. van Haesendonck, M. van der Auweraer, W. R. Salaneck, and M. Berggren, *Chem. Mater.* 2006, *18*, 4354.
[25] H. J. Lee, J. Lee and S. M. Park, *J. Phys. Chem. B.* 2010, *114*, 2660.
[26] B. Winther-Jensen, T. Knecht, C. Ong, J. Vongsvivut, C. Ong, N. Claark, *Macromol Mat. and Eng.* 2011, *296*, 2, 185.
[27] L. Jimison, A. Hama, X. Strakosas, V. Armel, D. Khodagholy, E. Ismailova, G. G. Malliaras, B. Winther-Jensen, M. R Owens, *J. Mater. Chem.* 2012, *22*, 19498.
[28] K. Zuber, M. Fabreto, C. Hall, P. Murohy, *Macromol. Rapid Commun.* 2008, *29*, 1503.
[29] M. Fabretto, M. Müller, K. Zuber, P. Murphy, *Macromol. Rapid Commun.* 2009, *30*, 1846.
[30] N. Massonnet, A. Carella, A. de Geyer, J. Faure-Vincent, J.-P. Simonato, Chem. Sci. 2015, 6, 412.
[31] M. N. Gueye, A. Carella, N. Massonnet, E. Yvenou, S. Brenet, J. Faure-Vincent, S. Pouget, F. Rieutord, H. Okuno, A. Benayad, R. Demadrille, J.-P. Simonato, Chem. Mater. 2016, 28, 3462.
[32] M. V. Fabretto, D. R. Evans, M. Mueller, K. Zuber, P. Hojati-Talemi, R. D. Short, G. G. Wallace, P. J. Murphy, Chem. Mater. 2012, 24, 3998
[33] K. Kiilerich-Pedersen, J. Daprà, S. Cherré, N. Rozlosnik, *Biosens Bioelectron.* 2013, *49*, 374.
[34] G. Rosati, J. Daprà, S. Cherré, N. Rozlosnik, *Electroanalysis*. 2014, *26*, 1400.